

The low-lying electronic states of FeO^+ : Rotational analysis of the resonance enhanced photodissociation spectra of the ${}^6\Pi_{7/2} \leftarrow X{}^6\Sigma^+$ system

Fernando Aguirre, John Husband, Christopher J. Thompson, Kay L. Stringer, and Ricardo B. Metz^{a)}

Department of Chemistry, University of Massachusetts, Amherst, Massachusetts 01003

(Received 27 June 2003; accepted 12 August 2003)

The resonance enhanced (1+1) photodissociation spectra of the (8,0) and (9,0) bands of the ${}^6\Pi_{7/2} \leftarrow {}^6\Sigma^+$ system of FeO^+ have been recorded. From a rotational analysis, the rotational parameters for the ${}^6\Sigma^+$ ground state of FeO^+ have been obtained for the first time. The rotational constant $B_0 = 0.5020 \pm 0.0004 \text{ cm}^{-1}$ is derived, giving $r_0 = 1.643 \pm 0.001 \text{ \AA}$. Other molecular parameters determined for the ${}^6\Sigma^+$ ground state are the spin-spin coupling constant, $\lambda = -0.126 \pm 0.006 \text{ cm}^{-1}$, and the spin-rotational coupling constant, $\gamma = -0.033 \pm 0.002 \text{ cm}^{-1}$. The assignment of the upper state as ${}^6\Pi_{7/2}$ is based on the characteristic appearance of the band and on time-dependent density functional (TD-DFT) calculations performed on FeO^+ . The reliability of the TD-DFT method in the prediction of excited states of FeO^+ is corroborated by calculations on CrF and MnO, which have been extensively characterized either by spectroscopy or by high-level theoretical calculations. © 2003 American Institute of Physics. [DOI: 10.1063/1.1615521]

I. INTRODUCTION

The spectroscopic study of first-row transition metal oxide cations (MO^+) is of great interest because of their ability to activate methane in the gas phase.¹⁻⁵ In particular, the reaction of FeO^+ with methane is both efficient and selective for the production of methanol. Under thermal conditions, the reaction occurs through two competitive pathways that lead to $\text{FeOH}^+ + \text{CH}_3$ (57%) and $\text{Fe}^+ + \text{CH}_3\text{OH}$ (41%). A minor pathway that leads to $\text{FeCH}_2^+ + \text{H}_2\text{O}$ (2%) has also been observed.¹ Higher collision energies favor FeOH^+ production, while the addition of buffer gas favors methanol production.³ Based on detailed density functional theory (DFT) and intrinsic reaction coordinate analyses, Yoshizawa *et al.*⁶⁻⁸ propose a two-step concerted mechanism for this reaction. The key intermediate $[\text{HO}-\text{Fe}-\text{CH}_3]^+$ can either dissociate to form FeOH^+ or isomerize to $\text{Fe}(\text{HOCH}_3)^+$, which dissociates to produce methanol. Several intermediates of the reaction have been studied by collision-induced dissociation⁹ and by photofragment spectroscopy.¹⁰

The study of low-lying electronic states of diatomic systems containing first-row transition metals has proven to be difficult due to the large number of electronic configurations derived from the occupancy of the $3d$ orbitals. However, despite difficulties in assigning the complicated spectra obtained, some experimental studies have been completed on $3d$ hydrides, halides, and oxides (MX , $\text{M}=\text{Sc}-\text{Cu}$, $\text{X}=\text{H}$, F , Cl , and O).¹¹⁻¹⁷ In 1986, Freiser and co-workers¹⁸ obtained the photodissociation spectrum of FeO^+ in an ion cyclotron resonance spectrometer using a lamp/monochromator with 10 nm resolution. In an earlier spectroscopy study of FeO^+ ,

we re-examined the predissociative ${}^6\Sigma \leftarrow {}^6\Sigma$ transition near 349 nm. The vibrational frequencies for both the ground and excited ${}^6\Sigma$ states were determined from the observed (0,0), (0,1), and (1,1) vibrational peaks.¹⁹ Although partially resolved rotational structure was observed in these vibrational peaks, full assignment of the ground state molecular parameters was not possible due to the limited lifetime of the predissociative ${}^6\Sigma$ state ($v'=0$, $\tau=3.5$ ps, $\Delta\nu=1.5 \text{ cm}^{-1}$). In the present paper, we study the lower-lying ${}^6\Pi \leftarrow {}^6\Sigma$ transition using resonance-enhanced (1+1) photodissociation. This technique overcomes the limit on resolution imposed by the dissociation lifetime of FeO^+ . The rotationally resolved structure recorded for this transition allows us to determine for the first time a set of molecular constants for the ${}^6\Sigma$ ground state of FeO^+ . Recently, Brucat and co-workers²⁰ used resonance-enhanced photodissociation to obtain the first rotationally resolved spectrum of CoO^+ , deriving rotational constants for the ${}^5\Delta_4$ ground state and the low-lying ${}^5\Pi_3$ and ${}^5\Phi_5$ excited states.

The high spin and large number of low-lying electronic states makes calculations of the electronic structure of transition metal oxides very challenging, usually requiring computationally expensive methods.²¹ However, during the last decade the excellent agreement between experimental results and calculations performed at the hybrid Hartree-Fock/density-functional (DFT) level has proven that DFT methods, in particular B3LYP, are effective and inexpensive tools for the prediction of molecular parameters of systems containing transition metal atoms.²²⁻²⁴ In addition, its application has been extended to the prediction of excited electronic states using time-dependent density functional theory (TD-DFT). However, to date, the prediction of excited electronic states using TD-DFT has been mostly restricted to closed-shell organic molecules,²⁵ and few calculations have been

^{a)} Author to whom all correspondence should be addressed, Electronic mail: rbmetz@chemistry.umass.edu; fax: +1-413-545-4490

performed on systems containing transition-metal atoms.^{26,27} In a recent TD-DFT study, Borowsky and Broclawik²⁶ predicted excited states of VO (⁴Σ⁻) and MoO (⁵Π) that are in excellent agreement with both experimental results and calculations performed at higher levels of theory. In the present study, we performed theoretical calculations on FeO⁺ using TD-DFT methods to complement the spectroscopic results and to obtain a better understanding of the electronic structure of FeO⁺. To test the reliability of the TD-DFT method on FeO⁺, we performed calculations on the isoelectronic MnO and CrF systems, which have been extensively characterized by both spectroscopy²⁸⁻³¹ and high level quantum calculations.³²

Besides its considerable interest as a model for methane activation, FeO⁺ is also important in the iron chemistry of the mesosphere,³³ where it is produced by the reaction of Fe⁺, introduced by meteorites, with ozone. Kopp *et al.*³⁴ estimated the concentration of atomic oxygen in the mesosphere using measured concentrations of Fe⁺, FeO⁺, and O₃, and the known rates for the Fe⁺ + O₃ and FeO⁺ + O reactions. In addition, the relatively high astronomical abundance of iron has led to considerable interest in the search for iron-containing molecules and ions in dense molecular clouds using radio astronomy.³⁵ The positive identification of molecules and ions in the interstellar medium requires the knowledge of accurate molecular parameters, especially rotational transition energies.³⁶ Recently, neutral FeO was tentatively identified in the interstellar medium, based on radio astronomy³⁷ and laboratory microwave spectra.³⁸ Thus, we hope that the rotational constants of FeO⁺ derived in this study stimulate microwave and radio astronomy studies of FeO⁺.

II. EXPERIMENTAL SECTION

The laser ablation photofragment spectrometer has been described in detail previously.¹⁹ Briefly, iron cations are generated by laser ablation of a rotating and translating rod (Fe, Sigma-Aldrich, 99.98% pure). Ablated Fe⁺ reacts with N₂O (Merriam-Graves, 99.8% pure) to produce FeO⁺ + N₂. Gas mixtures of 1%–2% N₂O and 5%–10% O₂ in helium were typically used with a backing pressure of 2 atm. Molecular oxygen was included in the mix to enhance vibrational and electronic cooling of the FeO⁺. Ions produced in the source expand supersonically into vacuum, then are skimmed, accelerated to 1800 V kinetic energy and rereferenced³⁹ to ground potential prior to entering the field-free flight tube. The photoexcitation of FeO⁺ is accomplished at the turning point of the reflectron using the fundamental output of a tunable Nd:YAG-pumped dye laser (0.08 cm⁻¹ linewidth). The charged dissociation fragments are identified by their subsequent flight times to a 40 mm diam dual microchannel plate detector. Photofragment spectra are obtained by monitoring the yield of Fe⁺ as a function of wavelength and normalizing to the parent ion signal at a constant laser power. The wavelength of the dissociation laser is calibrated using the known photoacoustic spectrum of water.⁴⁰ At the wavelengths used in this study, the photodissociation of FeO⁺ requires the absorption of two photons. A typical laser fluence of 150 mJ cm⁻² was used to produce a maximum dis-

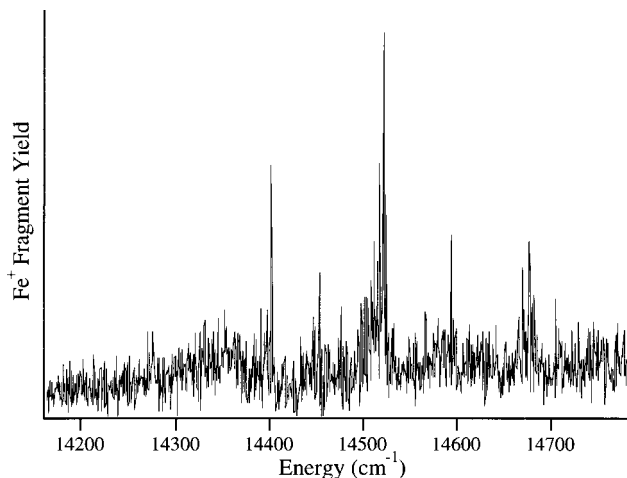


FIG. 1. Survey scan (step size ~ 1 cm⁻¹) of the resonance-enhanced (1+1) photodissociation FeO⁺ $\xrightarrow{h\nu}$ FeO⁺* $\xrightarrow{h\nu}$ Fe⁺ + O.

sociation yield of 1% at 689 nm. At higher laser fluences, up to 400 mJ cm⁻², the photodissociation spectrum of FeO⁺ becomes less resolved and the peak intensities are distorted. Laser power dependence studies are consistent with resonance-enhanced (1+1) photodissociation, in which the absorption of the first photon to a state below the dissociation limit is partially saturated. Excited ions then absorb an additional photon and dissociate.

III. COMPUTATIONAL DETAILS

All calculations were carried out using the B3LYP hybrid Hartree–Fock/density functional method as implemented in the GAUSSIAN 98 program package.⁴¹ Geometry optimizations and frequency calculations were performed using the diffuse 6-311+G(d,p) basis set on all the atoms. Single-point energy calculations at the optimized geometry were obtained using the 6-311+G(3df,2dp) basis set on oxygen, while the 6-311+G(d,p) basis set was retained for iron. The time-dependent density functional theory (TD-DFT) calculations were performed at the B3LYP level using the 6-311+G(d,p) basis set on all the atoms, except for FeO⁺, where no diffuse functions were added. Potential energy curves were constructed by scanning the M–X (M=Fe, Mn and Cr; X=O, F) bond length while performing TD calculations from the converged ground state density at each step. The internuclear distance is scanned until a poor description of the electronic transition, such as a negative vertical energy, is obtained in the TD-DFT calculation. A typical scan is carried out with a step size of 0.04 Å and usually covers a range of ± 0.3 Å from the optimized bond length of the system in its ground state. The calculated potential energy curves are subsequently fit to a Morse potential to derive the vibrational constants ($\omega_e, \omega_e x_e$) of each excited state.

IV. RESULTS AND DISCUSSION

A. Spectroscopy

Figure 1 shows a survey resonance-enhanced photodissociation spectrum of FeO⁺ between 14 150 and 14 800

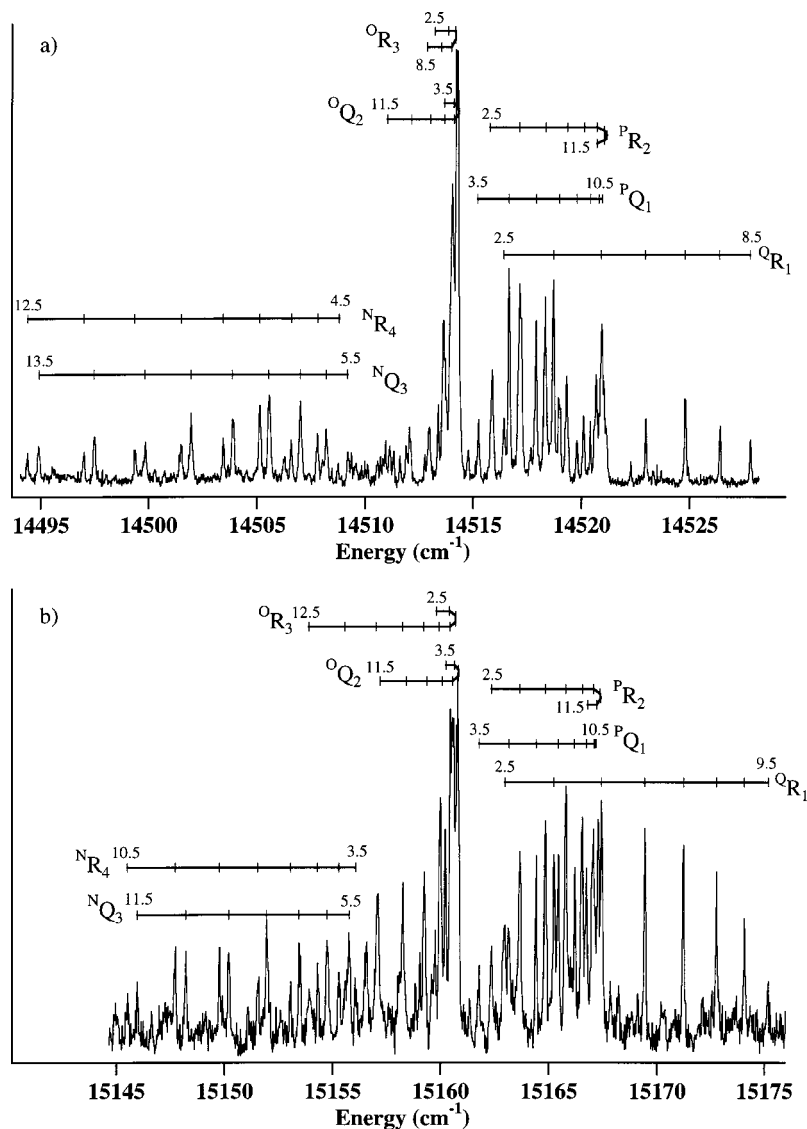


FIG. 2. Resonance-enhanced (1+1) photodissociation spectra and rotational assignments of the (a) (8,0) band and (b) (9,0) band of the ${}^6\Pi_{7/2} \leftarrow {}^6\Sigma^+$ system of FeO^+ . The subscripts indicate the spin component of the ${}^6\Sigma$ state (F_1 is $\Sigma=5/2$), while the superscripts indicate ΔN for the transition.

cm^{-1} . The spectrum consists of an intense band at $\sim 14\,500$ cm^{-1} and four less intense, neighboring bands. The average spacing between these bands is 65 cm^{-1} . Although this survey spectrum was also recorded at somewhat higher resolution, we concentrate our analysis on the most intense band, which is the only feature recorded with a high signal-to-noise level. Figure 2(a) shows the high-resolution spectrum of the intense band. The spectrum consists of approximate 50 rotational peaks distributed along a ~ 45 cm^{-1} region. Among the most significant features in this spectrum are the two band heads at $14\,514.3$ and $14\,520.9$ cm^{-1} . Considering that both band heads are shaded toward the red, the internuclear distance in the upper electronic state must be greater than that in the ground state ($B' < B''$), and therefore they correspond to either R or Q branches.⁴² Other distinguishing features of the spectrum are the isolated band and the progression of doublets observed at the high- and low-energy regions, respectively. The typical linewidth of an isolated peak in the spectrum is 0.08 cm^{-1} , our laser linewidth. The spectrum in Fig. 2(b) shows a similar, but less intense band that resides ~ 646 cm^{-1} to the blue of the most intense band. The strikingly similarity between the spectra in Figs. 2(a)

and 2(b) indicates that these rotational features are produced by transitions to two vibrational states in the same excited electronic state of FeO^+ . Therefore, to determine the absolute vibrational numbering of these transitions, we searched for the photodissociation of ${}^{54}\text{FeO}^+$ isotopomer. The small natural abundance of ${}^{54}\text{Fe}$ (5.8%) and low dissociation yield ($< 1\%$) make this experiment quite challenging. The photodissociation of ${}^{54}\text{FeO}^+$ gives a small peak at $14\,514.3$ cm^{-1} , which gives an isotopic shift of 21.1 cm^{-1} from the intense band head of ${}^{56}\text{FeO}^+$. Considering that under our experimental conditions FeO^+ ions are produced in their vibrationless ground state, the large isotopic shift indicates that high vibrational levels of the upper electronic state of FeO^+ are reached upon photoexcitation. On the basis of this isotopic shift and the vibrational frequency of the ground state of FeO^+ ($\nu_0'' = 838 \pm 4$ cm^{-1}) derived in an earlier study,¹⁹ the rotational features shown in Figs. 2(a) and 2(b) are tentatively assigned as the ($\nu' = 8 \leftarrow \nu'' = 0$) and ($\nu' = 9 \leftarrow \nu'' = 0$) bands, respectively. They will henceforth be referred to as the (8,0) and (9,0) bands.

The analysis of these bands was carried out in several steps. Since the ground state of FeO^+ is ${}^6\Sigma^+$ and the band

shown in Fig. 2(a) is the only intense feature observed between 14 300 and 14 700 cm⁻¹, a seemingly natural starting point to the analysis is that this band is derived from a ${}^6\Sigma \leftarrow {}^6\Sigma^+$ transition. The observation of a similar transition²⁹ for isoelectronic MnO supports this idea. However, this tentative assignment was revised when the rotational structure was examined closely and found to be incompatible with a ${}^6\Sigma \leftarrow {}^6\Sigma^+$ transition. Our second approach to the analysis is that these bands are due to a ${}^6\Pi \leftarrow {}^6\Sigma^+$ transition. Transitions to a ${}^6\Pi$ state are supported by TD-DFT calculations performed on FeO⁺, which are described in detail later in this paper. In the case of a ${}^6\Pi \leftarrow {}^6\Sigma^+$ transition, neighboring subbands due to transitions from the ${}^6\Sigma^+$ ground state to the spin-orbit components of the ${}^6\Pi$ state should be also observed. The spin-orbit splitting in the ${}^6\Pi$ state can be estimated using atomic parameters.⁴³ Assuming the spin-orbit interaction arises from an electron in the Fe 3*d* orbital, $A\Lambda\Sigma = \zeta_{3d}/2$, where ζ_{3d} is the atomic spin-orbit constant. Therefore, for the highest spin-orbit component of the ${}^6\Pi$ state ($\Sigma=5/2, \Lambda=1$), $A \approx \zeta_{3d}/5$. So, using $\zeta_{3d} = 416 \text{ cm}^{-1}$ for Fe⁺ gives $A = 83 \text{ cm}^{-1}$. This estimate is consistent with the average spacing of 65 cm⁻¹ observed between the bands in the low-resolution scan shown in Fig. 1.

${}^6\Pi \leftarrow {}^6\Sigma$ bands have been observed for several molecules, and their structure is fairly complex. The ${}^6\Sigma$ state is Hund's case (b) with rotational energy levels approximately given by⁴²

$$E_r'' = B''N''(N'' + 1). \quad (1)$$

Spin-spin (second-order spin-orbit) and spin-rotation interaction split the ${}^6\Sigma$ state into six spin-spin levels ($\Sigma=5/2, 3/2, 1/2, -1/2, -3/2$, and $-5/2$) and cause the energies to differ slightly from Eq. (1). The ${}^6\Pi$ state is Hund's case (a) and thus approximately has rotational energy levels,⁴²

$$E_r' = B'[J'(J' + 1) - \Omega'^2]. \quad (2)$$

Transitions can occur from each spin-spin level in the ${}^6\Sigma$ state to each spin-orbit level in the ${}^6\Pi$ state, leading to 18 branches for each spin-orbit state ${}^6\Pi_{\Omega}$, with expected intensities $R > Q > P$ for the rotational branches. The analysis of the rotational structure was started with the (9,0) band [Fig. 2(b)] because the branches are easier to pick out since more peaks are available. To start the analysis two branches were selected: the isolated peaks above 15 169 cm⁻¹ were assigned to an *R* branch, while those forming a head near 15 167 cm⁻¹ to a *Q* branch. Combination differences between these bands allows us to obtain the separation of successive rotational levels in the ground and excited states. The corresponding *P* branch was predicted to lie near 15 160 cm⁻¹, but it could not be confirmed because it is obscured by other branches. The assignment of the analogous features in the (8,0) band gives similar rotational energy levels for the ground state. Fitting the rotational energies to Eqs. (1) and (2) determines J' as well as J'' and N'' . Using $J'' = \Omega'' + N''$ allow us to obtain Ω'' . It is more difficult to determine Ω' . The lowest J' value observed places an upper limit on $|\Omega'|$ (as $J' \geq |\Omega'|$) but transitions to low J' are often overlapped by other peaks. The value of Ω' affects the overall intensity pattern and the extent of Λ doubling. These considerations, discussed in more detail below, strongly suggest $\Omega' = 7/2$. Thus, we assign these as the *Q* and *R* branches of the ${}^6\Pi_{7/2} \leftarrow {}^6\Sigma_{5/2}^+$ transition. As the ${}^6\Sigma$ states are numbered from F_1 ($\Sigma = 5/2$) to F_6 ($\Sigma = -5/2$), these are the PQ_1 and OR_1 bands, where the superscript indicates ΔN for the transition. As a next step, an additional branch located in the region between the two band heads of the spectrum was assigned. Using the rotational energy levels derived for the ground state facilitates assignment of the remaining peaks near 15 165 cm⁻¹ to the PR_2 branch (${}^6\Pi_{7/2} \leftarrow {}^6\Sigma_{3/2}$). The remainder of the spectrum exhibits a similar pattern with the red-shaded OQ_2 and OR_3 forming the sharp peak at 15 161 cm⁻¹ and the highly red-shaded NQ_3 and NR_4 extending

TABLE I. Experimental molecular constants (cm⁻¹) of the $X {}^6\Sigma^+$, ${}^6\Pi_{7/2}$, and (revised) ${}^6\Sigma$ states of FeO⁺, and the ${}^6\Sigma^+$ ground state of MnO.

Constant	FeO ⁺			MnO
	$X {}^6\Sigma^+$	${}^6\Pi_{7/2}$		$X {}^6\Sigma^{+b}$
	$v''=0$	$v'=8$	$v'=9$	$v''=0$
T_0	0	14 351.05	14 997.64	0
B	0.5020± 0.0004	0.3752± 0.0002	0.3720± 0.0002	0.489± 0.006 (0.484)
D^c	7×10^{-7}	4×10^{-7}	4×10^{-7}	
r (Å)	1.643± 0.001			1.664±0.01 1.647
λ	-0.126± 0.006			0.60±0.07 (0.7)
γ	-0.033± 0.002			-0.0024

^aMolecular constants in parentheses were estimated in an earlier one-photon spectroscopic study (Ref. 19) using the ground state molecular parameters of the isoelectronic MnO (Refs. 29–31) for the ground state of FeO⁺.

^bReference 31.

^cEstimated, but not fit.

TABLE II. Experimental and calculated (parentheses) line positions of the (8,0) band of the ${}^6\Pi_{7/2} \leftarrow {}^6\Sigma^+$ system of FeO^+ .

J''	R_1	R_2	R_4	Q_1	Q_3
2.5	14 516.43 (14 516.343)				
3.5	18.72 (18.670)	14 517.17 (14 517.141)		14 515.26 (14 515.190)	
4.5	20.94 (20.899)	18.33 (18.353)	14 508.75 (14 508.809)	16.66 (16.646)	
5.5	22.98 (22.942)	19.33 (19.361)	07.79 (07.831)	17.91 (17.917)	14 509.20 (14 509.190)
6.5	24.78 (24.774)	20.11 (20.154)	06.57 (06.612)	18.99 (18.976)	08.18 (08.218)
7.5	26.41 (26.387)	20.69 (20.726)	05.14 (05.154)	19.80 (19.815)	06.99 (07.009)
8.5	27.81 (27.772)	21.03 (21.07)	03.42 (03.460)		05.56 (05.567)
9.5			01.49 (01.533)		03.86 (03.892)
10.5			14 499.37 (14 499.372)		01.96 (01.986)
11.5			97.02 (96.979)		14 499.84 (14 499.850)
12.5			94.40 (94.353)		97.51 (97.480)
13.5					94.91 (94.882)

down to $15\,145\text{ cm}^{-1}$. Rotational constants are derived by nonlinear least squares fitting of the observed transition energies to the Hamiltonian,

$$\mathbf{H} = B(\mathbf{J} - \mathbf{S})^2 - D(\mathbf{J} - \mathbf{S})^4 + \gamma(\mathbf{J} - \mathbf{S})\mathbf{S} + (2/3)\lambda(3\mathbf{S}_z^2 - \mathbf{S}^2), \quad (3)$$

for the ${}^6\Sigma$ state and

$$\mathbf{H} = B(\mathbf{J} - \mathbf{S})^2 - D(\mathbf{J} - \mathbf{S})^4 + A\Lambda\Sigma + \mathbf{H}_{\text{LD}}, \quad (4)$$

$$\begin{aligned} \mathbf{H}_{\text{LD}} = & (o_v + p_v + q_v)(\mathbf{S}_+^2 + \mathbf{S}_-^2) - (p_v + 2q_v) \\ & \times (\mathbf{J}_+ \mathbf{S}_+ + \mathbf{J}_- \mathbf{S}_-) + q_v(\mathbf{J}_+^2 + \mathbf{J}_-^2), \end{aligned} \quad (5)$$

for the ${}^6\Pi$ state.

The Hamiltonians are diagonalized in a Hund's case (a) basis and transition intensities are obtained following the procedure outlined by Hougen.⁴⁴ Case (a) matrix elements

TABLE III. Experimental and calculated (parentheses) rotational lines of the (9,0) band of the ${}^6\Pi_{7/2} \leftarrow {}^6\Sigma^+$ system of FeO^+ . Additional lines included in the fit (with the predicted energy in parentheses): $R_3(11.5)$ 15 155.59 (15 155.576), $R_3(12.5)$ 15 153.90 (15 153.888), and $Q_4(4.5)$ 15 151.07 (15 151.112).

J''	R_1	R_2	R_4	Q_1	Q_3
2.5	15 162.98 (15 162.930)	15 162.36 (15 162.340)			
3.5	65.25 (65.227)	63.68 (63.697)	15 156.08 (15 156.088)	15 161.80 (15 161.777)	
4.5	67.45 (67.419)	64.85 (64.872)	55.29 (55.328)	63.17 (63.203)	
5.5	69.44 (69.417)	65.80 (65.836)	54.30 (54.306)	64.44 (64.437)	15 155.76 (15 155.710)
6.5	71.23 (71.198)	66.57 (66.578)	53.05 (53.036)	65.45 (65.450)	54.74 (54.692)
7.5	72.76 (72.752)	67.08 (67.091)	51.54 (51.520)	66.20 (66.239)	53.44 (53.433)
8.5	74.06 (74.073)		49.77 (49.761)	66.75 (66.795)	51.93 (51.933)
9.5	75.17 (75.162)		47.74 (47.764)		50.20 (50.192)
10.5			45.53 (45.524)		48.22 (48.217)
11.5					45.98 (46.002)

for a ${}^6\Sigma$ state have been reported by Gordon and Merer,²⁹ while those for the ${}^6\Pi$ state were derived following the definitions of Brown and Merer.⁴⁵

Table I gives the rotational constants obtained by fitting 36 unblended lines in the (8,0) band and 38 lines in the (9,0) band. Observed and calculated positions for all lines used in the fit are given in Tables II and III. Due to the low rotational temperature of the ion beam, the fit is quite insensitive to the centrifugal distortion constants. They were estimated⁴² using

$$D = \frac{4B^3}{\omega^2}, \quad (6)$$

and were not optimized in the fit. Including lambda doubling (H_{LD}) did not improve the fit, so it was not included in the final analysis. Lambda doubling is expected to be very small for low J values of a state with $\Omega=7/2$. The value of Ω' affects the calculated relative intensities of bands in the spectrum. Again, $\Omega'=7/2$ gives the best fit to observed intensities. P branch lines are predicted to be quite weak, and often lie under more intense branches. A vibrational spacing of $646.6 \pm 0.3 \text{ cm}^{-1}$ is derived for the ${}^6\Pi_{7/2}$ state from the determined origins of the (8,0) and (9,0) bands (Table I). Overall, excellent agreement is obtained between the calculated and experimental peak positions, with a root-mean square (rms) error of 0.03 cm^{-1} for the (8,0) and (9,0) bands of the ${}^6\Pi_{7/2} \leftarrow {}^6\Sigma^+$ system of FeO⁺.

The measured Fe–O distance of $r_0 = 1.643 \pm 0.001 \text{ \AA}$ is similar to the bond length of 1.647 \AA in isoelectronic MnO. Fiedler *et al.*⁴⁶ used multireference perturbation theory to calculate a bond length of 1.648 \AA for FeO⁺, in good agreement with our measurement. Our observation of transitions to $v'=8$ and 9 suggests that the Fe–O bond stretches significantly upon excitation to the ${}^6\Pi$ state. This is supported by the large change of the rotational constant, $\Delta B = 0.13 \text{ cm}^{-1}$, observed in the transition. The rotational simulations also predict a spin–spin coupling constant $\lambda = -0.126 \pm 0.006$ for the ${}^6\Sigma^+$ ground state. This spin–spin coupling constant is an effective constant that contains contributions from direct spin–spin coupling and second-order spin–orbit coupling: $\lambda = \lambda^{SS} + \lambda^{SO}$. The second-order spin–orbit coupling with nearby electronic states is expected to dominate λ_{eff} for molecules such as FeO⁺, which contain heavy atoms.^{31,43} However, the small value of λ for the ${}^6\Sigma^+$ ground state is a little unexpected when compared to that of the ${}^6\Sigma^+$ ground state of the isoelectronic MnO. It is possible that some contributions of off-diagonal second-order spin–orbit terms with opposite signs lead to this λ .

In an earlier study¹⁹ we measured a partially resolved ${}^6\Sigma \leftarrow {}^6\Sigma^+$ transition in FeO⁺ and obtained changes in rotational and spin–spin splitting constants (ΔB and $\Delta\lambda$) using B'' and λ'' for the isoelectronic MnO. With the constants derived in the present study, we can refine our analysis of the ${}^6\Sigma \leftarrow {}^6\Sigma^+$ band. The initial and revised parameters of the ${}^6\Sigma$ excited state of FeO⁺ are listed in Table I. The $\Delta r(\text{Fe–O})$ is almost unchanged, which is expected since the ground state bond lengths of FeO⁺ and the isoelectronic MnO are very similar. On the other hand, the change in the spin–spin coupling constant ($\Delta\lambda$) is produced by the significant difference

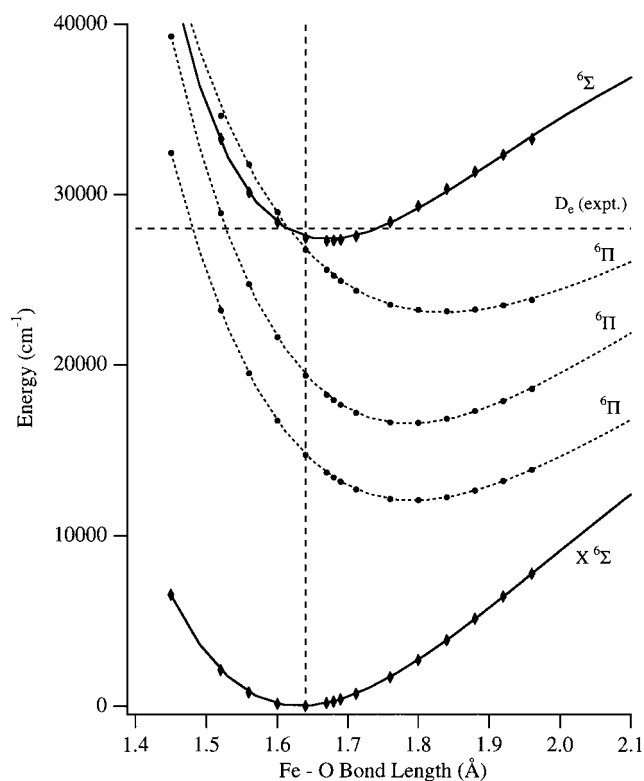


FIG. 3. Ground and several excited sextet states of FeO⁺. Symbols are the results of TD-DFT calculations. The solid (Σ states) and dotted (Π states) curves are Morse potentials fit to the calculated energies. The calculated r_e is indicated by the vertical line at 1.633 \AA , while the horizontal line shows the experimental $D_0 = 28\,000 \pm 400 \text{ cm}^{-1}$ (Ref. 47).

between the λ'' values of FeO⁺ and MnO. Although FeO⁺ and MnO are isoelectronic, it is expected that the difference in the total charge of these systems affects the relative energies of their electronic states,^{2,11} and hence the second-order spin–orbit interactions.

The rotational parameters for the ${}^6\Sigma^+$ ground state of FeO⁺ derived in this study (Table I) represent an excellent starting point for laboratory microwave spectroscopy of FeO⁺. Additional motivation for microwave studies comes from the recent tentative observation³⁷ of neutral FeO toward Sagittarius B2 *via* radio astronomy, which raises the possibility of detecting the cation. FeO⁺ is likely to be somewhat more challenging to detect than FeO for two reasons. First,

TABLE IV. Electronic states of FeO⁺ calculated using time-dependent density functional theory (TD-DFT).

State	T_e (cm ⁻¹)		r_e (Å)		$\omega_e/\omega_e x_e$ (cm ⁻¹)	
	TD	Exp.	TD	Exp.	TD	Exp. ^a
X ${}^6\Sigma^+$	0	0	1.633	1.638	853/5.4	849
${}^6\Sigma^+$	27 400	28 729	1.671	1.664	925/11.4	685
${}^6\Pi$	12 000	~9000 ^b	1.792		690/5.0	736
${}^6\Pi$	16 500		1.787		730/5.4	
${}^6\Pi$	23 100		1.837		603/4.3	

^aExperimental fundamental frequencies ν_0 have been converted to harmonic frequencies ω_e using the calculated (TD) $\omega_e x_e$ for each electronic state.

^bEstimated based on the origin of the (8,0) band ($14\,351 \text{ cm}^{-1}$) and the calculated ω_e and $\omega_e x_e$ values of the ${}^6\Pi$ state.

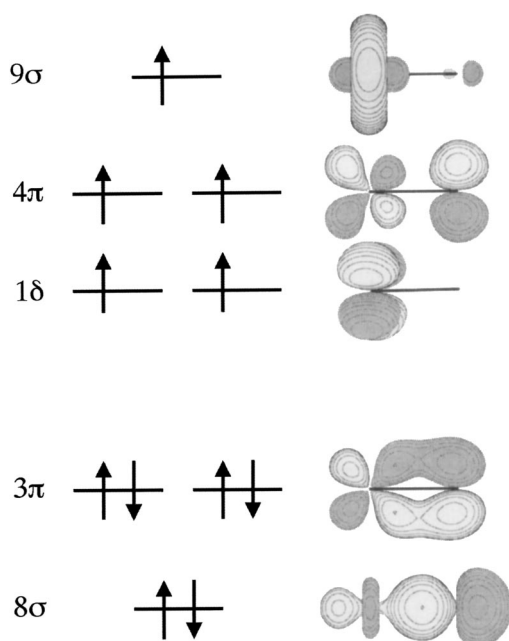


FIG. 4. Molecular orbitals of FeO^+ in its ${}^6\Sigma^+$ ground state configuration, from the B3LYP calculation at $r = 1.633 \text{ \AA}$.

FeO^+ is likely to be less abundant. Second, molecules will be distributed among more quantum states for FeO^+ than FeO . FeO has a ${}^5\Delta_4$ ground state. At 20 K the $J=5$ state (from which emission was tentatively detected) has $\sim 25\%$ of the population. The ${}^6\Sigma$ ground state of FeO^+ has sufficiently small spin–spin splitting that all six spin–spin levels are significantly populated, even at 20 K. At this temperature, the most populated rotational state only has 5% of the population. On a more positive note, the two species are calculated to have similar, large dipole moments of about 5 Debye. Also, in FeO^+ , states with the same value of N have transitions at similar energies, so the microwave transitions occur in multiplets, which simplifies confirming the carrier of an observed transition.

B. Calculations

To further explore the electronic structure of sextet states of FeO^+ we performed TD-DFT calculations on this system. Figure 3 shows calculated potentials of the ground and several excited electronic states of FeO^+ . The molecular parameters of these states are listed in Table IV. The resonant ${}^6\Pi \leftarrow {}^6\Sigma$ transition we observe corresponds to transitions to the

TABLE VI. Calculated TD-DFT electronic states of MnO .

State	T_e (cm^{-1})		r_e (\AA)		$\omega_e/\omega_e x_e$ (cm^{-1})	
	TD	Exp.	TD	Exp.	TD	Exp.
$X {}^6\Sigma^+$	0	0	1.637	1.644	866/5.1	843
$A {}^6\Sigma^+$	18 400	17 894	1.714	1.710	760/2.5	745

lowest ${}^6\Pi$ state in Fig. 3. The ${}^6\Sigma \leftarrow {}^6\Sigma$ band near 349 nm^{19} corresponds to transitions to the ${}^6\Sigma$ state near $27 400 \text{ cm}^{-1}$ in the figure. To illustrate the electronic transitions observed in our one-photon and resonance-enhanced (1+1) photodissociation studies of FeO^+ and predicted by TD-DFT, we use a simple molecular orbital picture that is commonly used to describe the electronic structure of diatomic molecules containing first-row transition metals. As shown in Fig. 4, the lowest-lying valence orbitals of FeO^+ are the 8σ and 3π orbitals. The 8σ orbital is predominantly ligand in character. The 3π orbitals have significant electron density on both atoms and are strongly bonding. Above these, but very close in energy, lie the nonbonding metal-centered 1δ , the weakly antibonding 4π , and the essentially nonbonding metal-centered 9σ orbitals. The lowest-unoccupied molecular orbital 10σ is mostly antibonding. In view of this description and the TD-DFT results, the first ${}^6\Pi$ excited state of FeO^+ arises from promoting an electron from the 3π Fe–O bonding orbital to the 1δ nonbonding orbital on the metal. Since this moves electron density from the oxygen to the metal, transitions to this electronic state have charge transfer character, and reduced bond order. The calculations predict a considerable increase in the bond length, as is observed. The transition to the ${}^6\Sigma$ excited state of FeO^+ near 349 nm corresponds to promoting an electron from the weakly bonding 8σ orbital to the essentially nonbonding 9σ orbital. Therefore, a small increase in the bond length is expected and observed.

To test the reliability of the TD-DFT methodology, we also performed calculations on the isoelectronic neutrals CrF and MnO . The results are listed in Tables V and VI, respectively. The results of the TD-DFT calculations performed on CrF are slightly worse than those obtained by Harrison *et al.*³² at the RCCSD(T) level of theory and slightly better than the values obtained by Bencheikh *et al.*²⁸ using the DFT ΔSCF schemes. Including FeO^+ , the bond lengths, excitation energies, and vibrational frequencies are calculated with a mean error of 0.03 \AA , 2000 cm^{-1} , and 50 cm^{-1} , respec-

TABLE V. Calculated TD-DFT electronic states of CrF .

State	T_e (cm^{-1})			r_e (\AA)			$\omega_e/\omega_e x_e$ (cm^{-1})		
	TD	Exp.	Other ^a	TD	Exp.	Other ^a	TD	Exp.	Other ^a
$X {}^6\Sigma^+$	0	0	0	1.807	1.784	1.783	620/3.9	664	679
$A {}^6\Sigma^+$	12 200	9953	9818	1.895	1.892	1.908	550/4.6	581	571
$B {}^6\Pi$	9900	8134	7551	1.864	1.828	1.831	564/4.3	629	632
			(10 136)			(1.818)			(699)

^aCalculations performed by Harrison *et al.* (Ref. 32) at the RCCSD(T) level of theory. The values in parentheses were obtained by Bencheikh *et al.* (Ref. 28) using the DFT ΔSCF scheme.

tively. The deviation in the calculated excitation energies is consistent with the 1500 cm⁻¹ deviation obtained by Borowski and Broclawik²⁶ in the prediction of excited states of VO and MoO using TD-DFT. Overall, the TD-DFT calculations give surprisingly accurate results, especially considering the small computational time required. One caveat is that the TD-DFT formalism is restricted to excited electronic states that are derived from a single excitation of the ground state configuration within a given manifold (alpha/beta). In addition, its application may not be reliable on systems that cannot be well described using a single determinant.

V. CONCLUSIONS

The (8,0) and (9,0) bands of the ${}^6\Pi_{7/2}\leftarrow{}^6\Sigma^+$ system of FeO⁺ have been studied by resonance-enhanced (1+1) photodissociation spectroscopy with rotational resolution. For the first time, a set of molecular parameters for the ${}^6\Sigma^+$ ground state of FeO⁺ is reported. The Fe–O bond length is determined to be 1.643±0.001 Å, while the spin–spin (λ) and the spin–rotational (γ) coupling constants are -0.126±0.006 and -0.033±0.002 cm⁻¹, respectively. Although the precision of the molecular parameters obtained in this study is not sufficiently high for a radioastronomy search for FeO⁺ in the interstellar medium, the results should greatly facilitate laboratory microwave studies of the ${}^6\Sigma^+$ ground state of FeO⁺. It is hoped that the present experiments will provide the motivation for future work in this area. We have computed excited states of FeO⁺, MnO, and CrF using the TD-DFT scheme. The excellent agreement between TD-DFT calculations and experimental and high-level calculations on these molecules indicates that TD-DFT is a reliable tool in predicting low-lying excited electronic states of small transition metal-containing systems.

ACKNOWLEDGMENTS

We would like to thank P. J. Brucat for helpful discussions regarding the assignment of the observed rotational structure of the ${}^6\Pi_{7/2}\leftarrow{}^6\Sigma^+$ system, W. M. Irvine for suggestions on astronomical observations, and O. Launila for providing a copy of his interactive fitting program (INFIA). Support for this work by a National Science Foundation Faculty Career Development Award is gratefully acknowledged.

¹D. Schröder and H. Schwarz, *Angew. Chem., Int. Ed. Engl.* **29**, 1433 (1990).

²D. Schröder and H. Schwarz, *Angew. Chem., Int. Ed. Engl.* **34**, 1973 (1995).

³D. Schröder, H. Schwarz, D. E. Clemmer, Y. Chen, P. B. Armentrout, V. Baranov, and D. K. Bohme, *Int. J. Mass Spectrom. Ion Processes* **161**, 175 (1997).

⁴D. Schröder, H. Schwarz, and S. Shaik, *Struct. Bonding (Berlin)* **97**, 91 (2000).

⁵R. B. Metz, *Adv. Phys.* **2**, 35 (2001).

⁶K. Yoshizawa, Y. Shiota, and T. Yamabe, *J. Chem. Phys.* **111**, 538 (1999).

⁷K. Yoshizawa, Y. Shiota, and T. Yamabe, *Chem.-Eur. J.* **3**, 1160 (1997).

⁸K. Yoshizawa, Y. Shiota, and T. Yamabe, *J. Am. Chem. Soc.* **120**, 564 (1998).

⁹D. Schröder, A. Fiedler, J. Hrusák, and H. Schwarz, *J. Am. Chem. Soc.* **114**, 1215 (1992).

¹⁰F. Aguirre, J. Husband, C. J. Thompson, K. L. Stringer, and R. B. Metz, *J. Chem. Phys.* **116**, 4071 (2002).

¹¹A. J. Merer, *Annu. Rev. Phys. Chem.* **40**, 407 (1989).

¹²R. S. Ram, C. N. Jarman, and P. F. Bernath, *J. Mol. Spectrosc.* **161**, 445 (1993).

¹³W. J. Balfour, O. Launila, and L. Klynning, *Mol. Phys.* **69**, 443 (1990).

¹⁴T. D. Varberg, J. A. Gray, R. W. Field, and A. J. Merer, *J. Mol. Spectrosc.* **156**, 196 (1992).

¹⁵T. Carter and J. M. Brown, *J. Chem. Phys.* **101**, 2699 (1994).

¹⁶T. Oike, T. Okabayashi, and M. Tanimoto, *J. Chem. Phys.* **109**, 3501 (1998).

¹⁷J. Lei and P. J. Dagdigian, *J. Chem. Phys.* **112**, 10221 (2000).

¹⁸R. L. Hettich, T. C. Jackson, E. M. Stanko, and B. S. Freiser, *J. Am. Chem. Soc.* **108**, 5086 (1986).

¹⁹J. Husband, F. Aguirre, P. Ferguson, and R. B. Metz, *J. Chem. Phys.* **111**, 1433 (1999).

²⁰A. Kamariotis, T. Hayes, D. Bellert, and P. J. Brucat, *Chem. Phys. Lett.* **316**, 60 (2000).

²¹J. F. Harrison, *Chem. Rev.* **100**, 679 (2000).

²²M. N. Glukhovtsev, R. D. Bach, and C. J. Nagel, *J. Phys. Chem. A* **101**, 316 (1997).

²³A. Ricca and C. W. Bauschlicher, Jr., *J. Phys. Chem. A* **101**, 8949 (1997).

²⁴C. J. Thompson, F. Aguirre, J. Husband, and R. B. Metz, *J. Phys. Chem. A* **104**, 9901 (2000).

²⁵K. B. Wiberg, R. E. Stratmann, and M. J. Frisch, *Chem. Phys. Lett.* **297**, 60 (1998).

²⁶T. Borowski and E. Broclawik, *Chem. Phys. Lett.* **339**, 433 (2001).

²⁷R. Farrell, J. V. Slageren, S. Zalis, and A. Vlcek, *Inorg. Chim. Acta* **315**, 44 (2001).

²⁸M. Bencheikh, R. Koivisto, and O. Launila, *J. Chem. Phys.* **106**, 6231 (1996).

²⁹M. Gordon and A. J. Merer, *Can. J. Phys.* **58**, 642 (1980).

³⁰A. G. Adam, Y. Azuma, H. Li, A. J. Merer, and T. Chandrakumar, *Chem. Phys.* **152**, 391 (1991).

³¹K. Namiki and S. Saito, *J. Chem. Phys.* **107**, 8848 (1997).

³²J. F. Harrison and J. H. Hutchison, *Mol. Phys.* **97**, 1009 (1999).

³³T. J. Kane and C. S. Gardner, *J. Geophys. Res.* **98**, 16875 (1993).

³⁴E. Kopp, P. Eberhardt, U. Hermann, and L. G. Bjoern, *J. Geophys. Res.* **90**, 13041 (1985).

³⁵J. C. Weingartner and B. T. Draine, *Astrophys. J.* **517**, 292 (1999).

³⁶T. J. Millar, C. M. Walmsley, C. Rebrion-Rowe, L. d'Hendecourt, S. Saito, and F. Rostas, *IAU Symp.* **197**, 303 (2000).

³⁷C. M. Walmsley, R. Bachiller, G. P. Des Forets, and P. Schilke, *Astrophys. J. Lett.* **566**, L109 (2002).

³⁸M. D. Allen, L. M. Ziurys, and J. M. Brown, *Chem. Phys. Lett.* **257**, 130 (1996).

³⁹L. A. Posey, M. J. DeLuca, and M. A. Johnson, *Chem. Phys. Lett.* **131**, 170 (1986).

⁴⁰M. Carleer, A. Jenouvrier, A. C. Vandaele *et al.*, *J. Chem. Phys.* **111**, 2444 (1999).

⁴¹M. J. Frisch, G. W. Trucks, H. B. Schlegel *et al.*, GAUSSIAN 98, Revision A.3 (Gaussian, Inc., Pittsburgh, PA, 1998).

⁴²G. Herzberg, *Molecular Spectra and Molecular Structure. I. Spectra of Diatomic Molecules* (Van Nostrand Reinhold Company, New York, 1950).

⁴³H. Lefebvre-Brion and R. W. Field, *Perturbations in the Spectra of Diatomic Molecules* (Academic, New York, 1986).

⁴⁴J. T. Hougen, *The Calculation of Rotational Energy Levels and Rotational Intensities in Diatomic Molecules*, N. B. S. Monograph 115, Washington, DC, 1970.

⁴⁵J. M. Brown and A. J. Merer, *J. Mol. Spectrosc.* **74**, 488 (1979).

⁴⁶A. Fiedler, D. Schröder, S. Shaik, and H. Schwarz, *J. Am. Chem. Soc.* **116**, 10734 (1994).

⁴⁷P. B. Armentrout and B. L. Kickel, in *Organometallic Ion Chemistry*, edited by B. S. Freiser (Kluwer Academic, Dordrecht, The Netherlands, 1994).